MetaPolar: A Low-Cost, Passive, mmWave Radar-Readable Metasurface Road Sign

Kai Zheng
University of California San Diego
kazheng@ucsd.edu

Wuqiong Zhao
University of California San Diego
wqzhao@ucsd.edu

Xinyu Zhang
University of California San Diego
xyzhang@ucsd.edu

Abstract

We present MetaPolar, a fully passive mmWave metasurface tag that enables robust Infrastructure-to-Vehicle (I2V) communication using standard automotive radars. Unlike conventional backscatter or spatial-encoding approaches, MetaPolar exploits the polarization domain: engineered split-ring resonators rotate the incident polarization to generate strong cross-polarized returns, while a crossed-dipole layer independently sculpts co- and cross-polarized amplitudes and phases. Through full-wave simulation, we build a codebook mapping metasurface layouts to distinct 2×2 polarimetric RCS signatures. A novel semi-retroreflective beam-shaping design maintains strong polarimetric contrast across a $\pm 7.5^\circ$ field of view, ensuring reliable decoding under realistic vehicle motion. We implement MetaPolar on low-cost FR-4 PCBs (< \$3 per tag) and validate it with a custom mmWave radar platform. Experiments demonstrate 2-bit encoding per tag (scalable to $2N$ bits with N tags), simultaneous multi-tag reading, and seamless integration into existing radar pipelines. Our results highlight MetaPolar's potential for cost-effective, scalable radar-readable signage in next-generation intelligent transportation systems.

1 Introduction

Vehicle-to-Everything (V2X) communication is a cornerstone of intelligent transportation systems, which creates an interconnected ecosystem to enhance road safety and traffic efficiency. A critical component of this ecosystem is Infrastructure-to-Vehicle (I2V) communication, where roadside units (RSUs) communicate with vehicles to convey information such as traffic signals, electronic signage, lane-marking sensors, and parking meters. The 5G Automotive Association (5GAA) forecasts mass rollout of 5G-V2X direct communications starting in Europe between 2026 and 2029, with other regions following suit as cellular infrastructure densifies [2]. However, critical challenges remain for the deployment and maintenance of V2I RSUs. Considering the millions of roadway intersects [6], the hardware cost and the maintenance cost skyrocket as more and more V2I infrastructure is being deployed.

One potential solution opportunity lies in Integrated Sensing and Communication (ISAC)–a core 6G candidate–also referred to as radar joint communications [42], where vehicles read information directly from unpowered roadside tags using only their onboard radar systems. This paradigm envisions a unified system where sensing and data exchange co-exist, saving hardware resources while unlocking new opportunities in smart transportation. Recent works have explored this vision by leveraging radar backscatter, where active or semi-passive tags reflect radar signals in controlled ways to convey information. For instance, Millimetro [32] uses Van Atta arrays to achieve long-range tag localization via retro-reflection, and BiScatter [24] modulates FMCW radar chirps to support two-way communication with passive IoT nodes. While capable, these tags require power sources and costly high-frequency components (*e.g.*, RF switches, specialized substrates), making their ubiquitous deployment on millions of road signs economically and logistically challenging. A more scalable approach is the use of fully passive, low-cost surfaces. RoS [22], for instance, introduced a passive metasurface that encodes information in its spatial radar cross-section (RCS) spectrum. However, RoS's spatial encoding scheme has a fundamental limitation: it requires a vehicle to perform continuous side-looking measurements while passing the sign to decode the information, which constrains the detection range and complicates the reading process. Furthermore, distinguishing any passive tag from common urban objects remains a significant challenge. Existing systems often have to resort to additional visual/optical sensors and real-time location/mapping information [22].

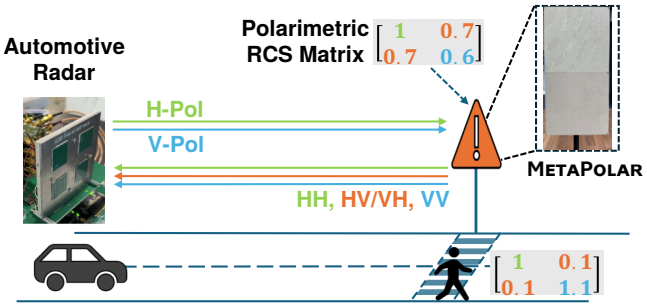

Figure 1: The MetaPolar road sign is designed to exhibit a reflection signature identifiable by mmWave automotive radars, encoding information in the 2×2 polarimetric radar cross section (RCS) matrix.

In this paper, we present MetaPolar, a new class of passive, easily fabricable mmWave metasurface tags that enable robust, high-capacity, radar-readable I2V communication. MetaPolar explores a fundamentally different design axis by leveraging radar polarimetry–the ability of mmWave radars to resolve and interpret the polarization state of reflected signals. Such polarization diversity is widely employed in 5G communication systems through dual-polarized phased arrays [1, 10, 11], and this hardware feature is anticipated to remain in 6G ISAC systems. Instead of modulating radar reflections spatially or temporally, MetaPolar uses an engineered metasurface tag to passively control both co- and cross-polarized returns, as illustrated in Fig. 1. This method enables a

SenSys '26, Saint Malo, France

ACM ISBN 979-8-4007-2309-4/2026/05
https://doi.org/10.1145/3774906.3800464

passive tag to stand out in radar scenes dominated by environmental scatterers, which reflect radar signals with minimal polarization change. Furthermore, it allows MetaPolar to engineer the relative amplitude and phase across polarization channels to create distinguishable polarimetric radar cross section (RCS) patterns, effectively encoding multiple bits of information per tag.

Realizing this system, however, involves several technical challenges, particularly in practical V2I settings. First, engineering a passive metasurface that provides consistent polarization transformation at mmWave frequencies requires precise subwavelength patterning and control of surface currents. Second, the encoding must remain robust under varying radar angles and environmental conditions. It entails a semi-retroreflective design that balances directivity and coverage. Third, decoding must be achievable from a single radar sweep using only the radar's native signal processing pipeline, without requiring tag movement, multiple observations, or custom waveforms.

We address these challenges through a tightly integrated hardware–signal–processing co-design, which combines electromagnetic metasurface engineering with polarimetric radar decoding to push the boundaries of passive tag communication. At the core of MetaPolar is an electromagnetic structure that comprises two custom-engineered metasurfaces: *(i)* an array of split-ring resonators (SRRs) that rotate the polarization of incident mmWave signals, enabling strong cross-polarized reflections; and *(ii)* a patterned layer of crossed dipoles whose geometry and orientation selectively control the relative amplitude and phase across co- and cross-polarized RCS channels. Together, these metasurfaces form a composite tag that can generate distinct polarimetric signatures in response to automotive radar beams. The design process is grounded in full-wave electromagnetic simulation and optimization, where we parameterize the SRR and dipole layouts across frequency, incidence angle, and polarization to build a codebook of signature states. This codebook defines an efficient and predictable mapping from metasurface layout to bit values.

To ensure readability under realistic deployment conditions, we introduce a novel semi-retroreflective beam shaping technique in the metasurface layout. Unlike conventional retroreflectors that rely on geometric symmetries (*e.g.*, Van Atta arrays [22]), our approach uses spatially varied dipole phase profiles to sculpt the backscattered beamwidth. This produces a controlled angular spread in reflected energy that maintains strong polarimetric contrast over a reasonably wide field of view–a critical requirement for vehicular settings where radar angles vary rapidly due to road curvature.

On the radar side, MetaPolar departs from traditional backscatter decoding by shifting the burden of signal extraction to the polarimetric domain. We develop a radar processing pipeline that operates directly on the full 2×2 scattering matrix captured by quad-polarized phased arrays, extracting both magnitude and relative phase across HH, VV, HV, and VH channels. Each MetaPolar tag is designed to occupy a distinct location in this four-dimensional RCS space, enabling both robust identification and bit-level decoding from a single radar sweep. Unlike spatial encoding schemes that rely on object position or beam scanning, MetaPolar's signatures are localized in the polarimetric spectrum, making them resilient to multipath and environmental clutter. We further augment the pipeline with calibration routines that compensate for hardware phase drift and antenna gain imbalance, ensuring stable decoding over extended use. This system requires no tag movement, no active modulation, and no changes to the radar's waveform–only the use of standard radar captures with polarimetric post-processing.

We have implemented and validated MetaPolar using low-cost FR-4 PCB fabrication with a cost of under $3 per tag. To evaluate the system, we use a mmWave radar platform with commercial-off-the-shelf phased arrays. Our experiments demonstrate encoding of 2 bits per tag—and $2N$ bits using N tags in proximity, with reliable decoding over a $\pm 7.5^\circ$ angular range. The system allows for simultaneous reading of multiple signs and integrates seamlessly into standard automotive radar processing pipelines.

In summary, this paper makes the following key contributions:

- We propose a novel, fully passive, and low-cost mmWave radar-readable sign, MetaPolar, which encodes information in the polarimetric RCS matrix, enabling robust communication with forward-facing radars.
- We develop a polarimetric scattering matrix engineering framework based on a decoupled metasurface design that allows for independent control of co- and cross-polarization channels to scale up encoding capacity.
- We implement the MetaPolar design using cost-effective fabrication methods and comprehensively validate its performance in practical settings, demonstrating robust and scalable encoding, wide-angle readability, and seamless integration with radar systems.

2 A Primer on Radar Polarimetry

Radar polarimetry is a sensing technique that leverages the transmission and reception of electromagnetic waves with varying polarization states to characterize the scattering behavior of targets. By comparing how different polarizations are reflected or transformed by a target, radar polarimetry provides rich information about the target's shape, orientation, surface texture, and material composition. Polarization has been widely adopted by mmWave transceivers to improve channel diversity [1, 10, 11], and such transceivers are expected to continue to be used in 6G ISAC systems. When comprising horizontal (H) and vertical (V) channels at both transmit and receive ends, the interaction between the radar signal and the target can be captured using a polarimetric scattering matrix:

$$\sigma = \begin{bmatrix} \sigma_{HH} & \sigma_{VH} \\ \sigma_{HV} & \sigma_{VV} \end{bmatrix}, \tag{1}$$

where each element σ_{pq} represents the complex radar cross-section (RCS) corresponding to a signal transmitted with polarization $q \in \{H, V\}$ and received with polarization $p \in \{H, V\}$. To empirically understand the polarimetric scattering behavior of common environmental objects at mmWave frequencies, we use a 60 GHz programmable radar platform (Sec. 5) to characterize various daily objects in real-world roadway settings. Tab. 1 compiles the polarimetric scattering matrices, where the elements are normalized to the σ_{HH} component to facilitate direct comparison across objects.

Theoretical analysis [16, Chap. 3.6] has shown the ideal scattering matrix for targets with various shapes (plate, sphere, trihedral, dipole, *etc.*). Our experimental results are generally aligned with the theory. Specifically, planar objects (like plastic signs) exhibit strong and nearly equal co-polarization terms (HH and VV) and

Table 1: Scattering matrices of common roadway objects.

Object	|HH|	|HV|	|VH|	|VV|
Plastic Sign	1	0.06	0.05	1.02
Cylinder Pole	1	0.09	0.03	0.84
Square Pole	1	0.01	0.04	0.77
Human	1	0.03	0.09	1.21
Tree-1	1	0.13	0.14	0.67
Tree-2	1	0.05	0.06	0.50
Car	1	0.10	0.09	0.78

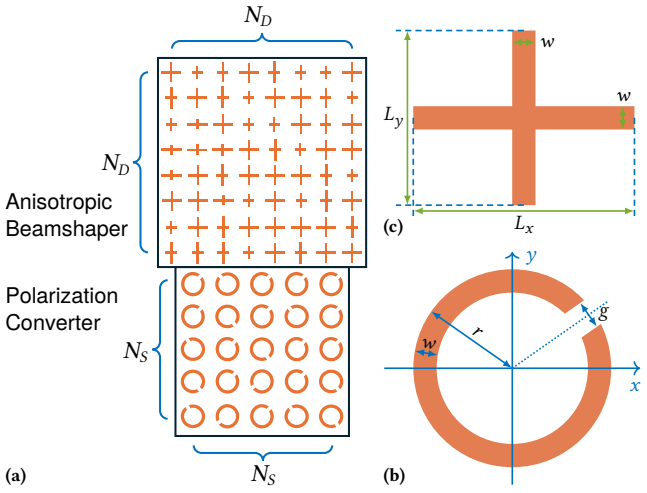

Figure 2: MetaPolar design. (a) MetaPolar comprises two concatenated sub-metasurfaces: the polarization converter, based on (b) split-ring resonators (SRR); and the anisotropic beam shaper, based on (c) crossed-dipoles (XD).

very weak cross-polarization terms (HV and VH). Dipole-shaped objects (*e.g.*, cylinder pole, square pole) show similar results except that the HH channel is stronger than VV channel. In contrast, more structurally complex objects, such as trees with irregular branches, exhibit noticeably stronger cross-polarized returns. These arise from depolarization effects introduced by multiple scattering paths and geometric randomness [36].

However, all the common objects exhibit a low *polarization conversion ratio* (HV/HH < 0.2). This inspires us to engineer artificial metasurface tags with strong cross-polarization terms that can be easily distinguished by a polarimetric radar. Furthermore, by controlling the amplitude and phase response of a metasurface's scattering matrix, we can embed information into both the co- and cross-polarized channels. Notably, in monostatic radar configurations–where the transmit and receive antennas are co-located–the HV and VH channels are theoretically reciprocal and thus convey redundant information. Therefore, it suffices to focus on three independent channels (HH, VV, HV) when designing and decoding the polarimetric tag responses.

3 MetaPolar Design

3.1 System Overview

The polarimetric scattering matrix of the metasurface tag, as perceived by the radar, is essentially determined by the reflection strength and the phase towards the radar direction. To encode information into this matrix, the metasurface must achieve two functions: polarization conversion and reflection beamforming. Polarization conversion creates σ_{VH} and σ_{HV} in the polarization matrix (Eq. (1)), and the degree of polarization conversion must be carefully controlled. Meanwhile, beamforming controls the amplitude and the phase of the polarimetric RCS terms. Both must work together to achieve polarimetric RCS engineering.

Achieving independent control of the cross-polarization and co-polarization channels within the same unit-cell structure is non-trivial. MetaPolar circumvents this complication with a decoupled design, comprising two co-located sub-metasurfaces: the polarization converter and the anisotropic beamshaper, as shown in Fig. 2a. The polarization converter aims to rotate the polarization mode of the EM wave to its orthogonal mode, while the anisotropic beam shaper can independently engineer the reflection beam pattern of two orthogonal co-polarized channels, namely HH and VV. These two sub-metasurfaces are placed in proximity such that, from the radar's perspective, they appear as a single scatterer due to the radar's limited angular resolution. As a result, the radar observes a composite scattering matrix, which is approximately the sum of the individual RCS matrices contributed by each sub-metasurface.

Encoding information into the polarimetric RCS is challenging in practice. Environmental factors such as multipath fading, unknown path loss, and the extreme phase sensitivity of mmWave signals can distort the perceived radar signatures. Moreover, small fabrication imperfections or misalignments may result in non-ideal retro-reflection patterns. To address these constraints, MetaPolar encodes data across two selected dimensions of the RCS matrix: (1) the amplitude of cross-polarized components; and (2) the relative phase between co-polarized channels. These orthogonal encoding channels increase the available symbol space while improving robustness under varying radar angles and environmental conditions.

3.2 Unit Cell Design

To realize the distinct polarimetric signatures required for information encoding, MetaPolar constructs its two sub-metasurfaces using different electromagnetic unit cells, each optimized for a specific scattering behavior.

3.2.1 Split Ring Resonator (SRR). MetaPolar's polarization converter employs split ring resonators (SRRs) as the unit cell. An SRR comprises a conductive ring with a split gap, as shown in Fig. 2b. The *split angle* α determines the degree of polarization conversion. The scattering matrix of a single SRR with a split angle of α can be written as follows [30]:

$$\sigma(\alpha) = \begin{bmatrix} \cos 2\alpha & \sin 2\alpha \\ \sin 2\alpha & -\cos 2\alpha \end{bmatrix}. \tag{2}$$

Therefore, when α equals 45°, 135°, 225°, and 315°, a maximum polarization conversion ratio is achieved. These configurations correspond to diagonal symmetries that optimally couple the incident polarization to its orthogonal counterpart. In addition, when the sign in $\sigma(\alpha)$ changes, the phase is also flipped by 180°. Tab. 2 shows the impact of α on the phase.

Table 2: Phase change of SRR with different split angles.

α	0–45°	45°–90°	90°–135°	135°–180°
HH	−90°	90°	90°	−90°
VV	90°	−90°	−90°	90°
HV/VH	−90°	−90°	90°	90°

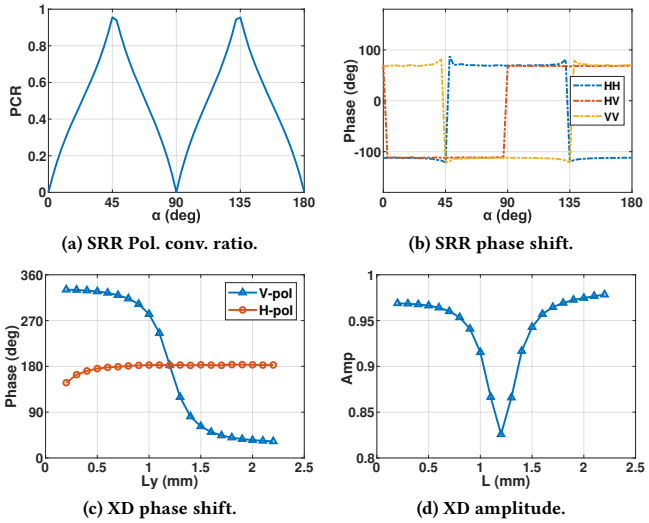

(a) SRR Pol. conv. ratio.

(b) SRR phase shift.

(c) XD phase shift.

(d) XD amplitude.

Figure 3: The simulation results in Ansys HFSS. The split angle α of the SRR controls both the (a) polarization conversion ratio and the (b) phase shift for orthogonal polarization modes. (c) and (d) show the relationship between phase and amplitude with the dipole length of XD.

Therefore, SRR can achieve a 1-bit phase shift effect. The phases of HV/VH and VV/HH can be decoupled and selected independently, while HH and VV always have a 180° phase shift.

To achieve a high polarization conversion ratio, the resonance frequency of SRR must be close to the radar's operating frequency. The SRR can be modeled as an L-C resonance circuit, and its resonance frequency is determined by its geometric parameters (radius r, width w, and the gap g) as shown in Fig. 2b. Following common practice, we fine-tune these dimensions using full-wave electromagnetic simulation tools to match the desired resonance frequency.

3.2.2 Crossed Dipoles (XD). To modulate the co-polarized radar returns, *i.e.*, σ_{HH} and σ_{VV}, MetaPolar's anisotropic beamshaper employs crossed-dipole (XD) unit cells, each consisting of two orthogonal dipoles with independently variable lengths L_x and L_y (Fig. 2c). Each dipole acts as a resonant reflector for its respective polarization axis. By adjusting its length, we can finely control the phase and amplitude of the reflected signals in that polarization.

Electromagnetic simulations show that varying the length of a dipole from 0.2 mm to 2.2 mm enables a phase shift spanning nearly the entire 360° range. (Fig. 3c). Notably, the length variation at one direction (H) has a negligible impact on the orthogonal (V) polarization direction. This decoupling enables independent assignment of phase states to the HH and VV elements of the scattering matrix.

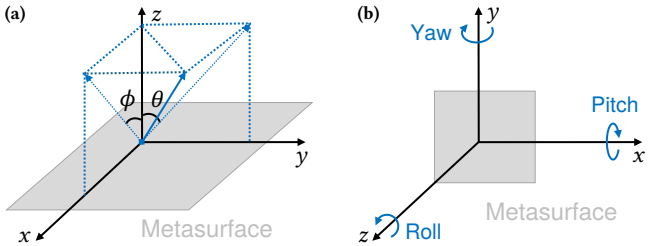

Figure 4: Definitions used in MetaPolar: (a) The coordinate system and (b) the definition of Yaw, Roll, and Pitch axes.

3.3 Semi-Retroreflective Beam Pattern Design

To ensure the passive road sign can be reliably detected by radar, the reflecting pattern should ideally be retro-reflective, providing the maximum reflection gain. While retro-reflectiveness can be achieved using 1D Van-Atta arrays (VAAs) [22] or Luneburg lens [26], it is difficult to achieve using a 2D planar metasurface. This is because of the contradictory phase shift requirement of different incident angles. A set of phase shifter values that satisfy retroreflectiveness at an incident angle (θ, ϕ) do not retroreflect the EM-wave at the incident angle $(\theta, -\phi)$. Therefore, we make compromises on the perfect retro-reflectiveness and aim to maximize the retro-reflective gain as much as possible within a given angle range.

3.3.1 Formulation of the Optimization Problem. Consider a metasurface with N elements, each of which has a complex RCS of $a_m e^{j\varphi_m}$, located at $\mathbf{p}_m = (x_m, y_m)$. The far-field gain at with reflected angle (ϕ_r, θ_r) and incident angle (ϕ_i, θ_i) can be written as:

$$F(\phi_i, \theta_i, \phi_r, \theta_r; \{\varphi_m\}) = \sum_{m=1}^{N} a_m e^{j\varphi_m} \cdot e^{j\frac{2\pi}{\lambda}\mathbf{p}_m \mathbf{e}_i} \cdot e^{j\frac{2\pi}{\lambda}\mathbf{p}_m \mathbf{e}_r}, \quad (3)$$

$$\mathbf{e}_i = (\sin\theta_i, \sin\phi_i)^T, \quad \mathbf{e}_r = (\sin\theta_r, \sin\phi_r)^T. \quad (4)$$

With $(\phi_r, \theta_r) = (\phi_i, \theta_i)$ for retro-reflectiveness, the gain can be written as:

$$F(\phi_i, \theta_i; \{\varphi_m\}) = \sum_{m=1}^{N} a_m e^{j(\varphi_m + \frac{4\pi}{\lambda}\mathbf{p}_m \mathbf{e}_i)}. \quad (5)$$

The design goal of the metasurface is to maximize the retro-reflective gain G in the angles of interest. To this end, we formulate the unit cell optimization problem as follows:

$$\arg\min_{\{\varphi_m\}} L(\{\varphi_m\}) := \sum_{l=1}^{K} w_l |F_l(\{\varphi_m\}) - G_l|^2. \quad (6)$$

Here, $l = 1, \ldots, K$ indices the discretized angles, and w_l is a weight factor. The target gain G_l can be selected as flat for the defined angle range. The maximum possible gain is the coherent combination of the reflected signal from all the unit cells, which equals N. Therefore, we define

$$|G_l| = \alpha N, \forall\, l, \quad (7)$$

where $0 < \alpha \leq 1$ is a scaling factor that relaxes the requirement for perfect retro-reflectiveness.

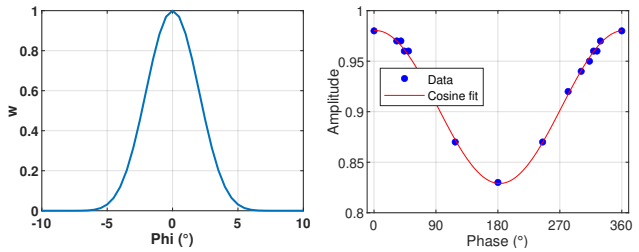

(a) $w(\phi)$, $P = 10$. **(b)** $g(\varphi)$, $\tan\delta = 0.02$.

Figure 5: (a) The weight function; (b) The amplitude-phase relationship of dipole.

Given an angle range: $-\theta_{\max} < \theta < \theta_{\max}$ and $-\phi_{\max} < \phi < \phi_{\max}$, we define $w(\theta, \phi)$ using the following equation:

$$w_l = [\cos(\frac{\pi}{2}\frac{\phi_l}{\phi_{\max}})]^P [\cos(\frac{\pi}{2}\frac{\theta_l}{\theta_{\max}})]^Q. \tag{8}$$

This weight function places a stronger emphasis on angles close to 0 degrees, which are the most critical regions for retro-reflectiveness. $Q > 1$ and $P > 1$ are parameters that define the degree of emphasis. An example of the weight function is shown in Fig. 5a.

3.3.2 Solving the Optimization Problem. To compute the gradient of the loss function in Eq. (6) over the phase of each unit cell φ_m, we must first know the mapping function $a = g(\varphi)$. For the SRR, the amplitude is constant for different split angles; therefore, we set $a = 1$. For the XD, each phase can be mapped to amplitude one by one using the simulation result in Fig. 3d. We fit the mapping with a cosine function to facilitate loss and gradient computing.

$$g(\varphi) = a + b\cos(\varphi - c). \tag{9}$$

The fitted $g(\varphi)$ function is shown in Fig. 5b.

Define $f_{m,l} = e^{j(\varphi_m + \frac{4\pi}{\lambda}\mathbf{p}_m\mathbf{e}_l)}$, for each angle l, the derivative of the loss can be computed as below:

$$\frac{\partial E_l}{\partial \varphi_n} = 2\Re\left\{(F_l - G_l)^*(j + \frac{g'(\varphi_n)}{g(\varphi_n)})f_{n,l}\right\}. \tag{10}$$

Summing over all angles, the total gradient for φ_n is

$$\frac{\partial L}{\partial \varphi_n} = \sum_{l=1}^{K} w_l \frac{\partial E_l}{\partial \varphi_n}. \tag{11}$$

With the gradient formulation, the phase shift of the unit cells can be optimized with the quasi-Newton method. Examples of the optimized retro-reflective pattern are displayed in Fig. 6a to 6d.

3.4 Information Encoding

The complex polarimetric RCS of the metasurface (σ_{HV}, σ_{HH}, and σ_{VV}) perceived by the radar can be written as follows:

$$\begin{cases} S_{HV} = a\,e^{j\phi_X}\,\sigma_{HV} + n_X, \\ S_{HH} = a\,e^{j\phi_C}\,\sigma_{HH} + n_H, \\ S_{VV} = a\,e^{j\phi_C}\,\sigma_{VV} + n_V. \end{cases} \tag{12}$$

$a\,e^{j\phi_X}$ and $a\,e^{j\phi_C}$ are the gains of the backscatter channels. n_X, n_H, and n_V denote the noises independent over the channels, which can be modeled as complex Gaussian random variables following $CN(0, \sigma^2_{noise})$.

The amplitude a is common to all three channels due to the similar distances to the radar. However, the phase of the co-polarization channel (ϕ_X) and that of the cross-polarization channel (ϕ_C) can be different because of the concatenation design of the polarization converter and anisotropic beamshaper (Sec. 3.1), making the distances to the radar not always the same. Since the HH and VV channels share the same unit cell array, any common gain/phase change due to backscattering channel fading, imperfection in metasurface fabrication, *etc.* will have equal contribution to both channels; therefore, their channel phases can be modeled as the same.

As the backscatter channel gain is difficult to estimate in practice, we cannot directly encode information using the absolute value. Instead, we encode information in the *relative strength* of the RCS matrix, using either the HH channel or the VV channel as a reference. We thus compute the ratio of the complex RCS between the interrogated channel (i) and the reference channel (r):

$$R = \frac{a\,e^{j\phi_i}\sigma_i + n_i}{a\,e^{j\phi_r}\sigma_r + n_r}. \tag{13}$$

The interrogated channel can be either the cross-polarization channel ($\sigma_i = \sigma_{HV}$) or the other co-polarization channel ($\sigma_i = \sigma_{HH}$).

For high SNR scenarios (*i.e.* $|a\,e^{j\phi}\sigma| \gg |n|$), we have:

$$\begin{aligned} R &= \frac{\sigma_i\,e^{j\phi_i}}{\sigma_r\,e^{j\phi_r}}\frac{1 + \frac{n_i}{a\,\sigma_i\,e^{j\phi_i}}}{1 + \frac{n_r}{a\,\sigma_r\,e^{j\phi_r}}} \approx \frac{\sigma_i\,e^{j\phi_i}}{\sigma_r\,e^{j\phi_r}}(1 + \frac{n_i}{a\sigma_i\,e^{j\phi_i}} - \frac{n_r}{a\sigma_r\,e^{j\phi_r}}) \\ &= \frac{\sigma_i}{\sigma_r}e^{j(\phi_i - \phi_r)} + \frac{n_i}{a\,\sigma_r}e^{-j\phi_r} - \frac{\sigma_i\,n_r}{a\,\sigma_r^2}e^{j(\phi_i - 2\phi_r)}. \end{aligned} \tag{14}$$

Eq. (14) indicates that R is approximately Gaussian distributed with mean $\frac{\sigma_i}{\sigma_r}e^{j(\phi_i - \phi_r)}$ and variance $\frac{\sigma_i^2 + \sigma_i^2}{a^2\sigma_r^4}\sigma^2_{noise}$.

For the S_{HV}/S_{VV} channel, since $(\phi_i - \phi_r)$ is unknown and varies over different read angles, we can only encode information in the amplitude of $\frac{\sigma_i}{\sigma_r}$. For S_{HH}/S_{VV}, $(\phi_i - \phi_r)$ is canceled out, and we can theoretically encode information both on the amplitude and the phase. In MetaPolar, we encode information in the amplitude of $|S_{HV}/S_{VV}|$ and the phase of $\angle(S_{HH}/S_{VV})$.

3.4.1 Amplitude Encoding. Although one could encode data in the co-polarization amplitude ratio $|S_{HH}/S_{VV}|$, environmental clutter often renders this channel unreliable. By contrast, few natural reflectors exhibit significant polarization conversion, so the cross-polarization ratio $|S_{HV}/S_{VV}|$ is inherently more stable. Consequently, MetaPolar performs amplitude encoding exclusively on the cross-polarization channel.

Because a reflector's RCS scales with its illuminated area, a straightforward approach is to vary the number of active elements on the metasurface to adjust absolute reflection strength. In practice, however, retro-reflective gain does not scale linearly with element count due to beamforming interactions. To maximize the relative amplitude contrast over our target angular sector, we therefore apply the optimization framework from Sec. 3.3. In particular, we sweep the parameter α in Eq. (7) to synthesize multiple discrete amplitude states within the designed field of view.

3.4.2 Phase Encoding. To control the phase of HH/VV, we aim to create a constant relative phase difference on the retro-reflective gain over a wide angle range. To achieve this, we set different optimization goals for the reference channel (VV) and the interrogated

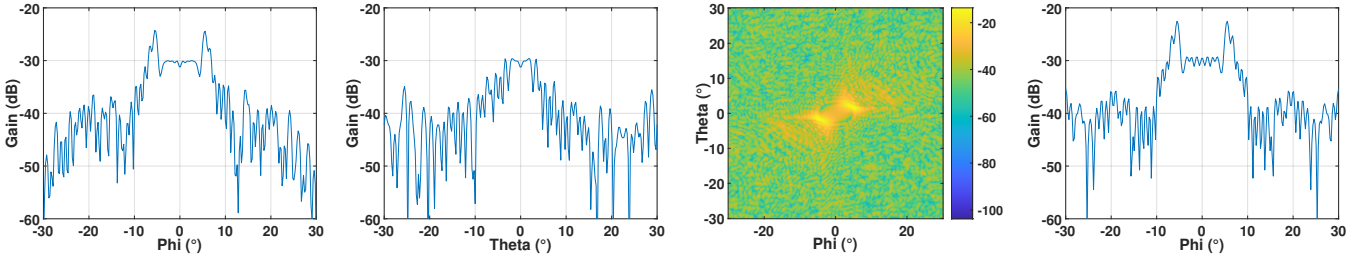

(a) Horizontal. (b) Vertical. (c) 2D. (d) Horizontal, 1-bit quantized.

Figure 6: Simulated Gain Pattern. (a)–(c) retro-relective pattern with $\alpha = -25$ dB, $\phi_{max} = 10°$, $\theta_{\max} = 5°$, $P = 30$, and $Q = 20$. (d) 1-bit quantized pattern with SRR.

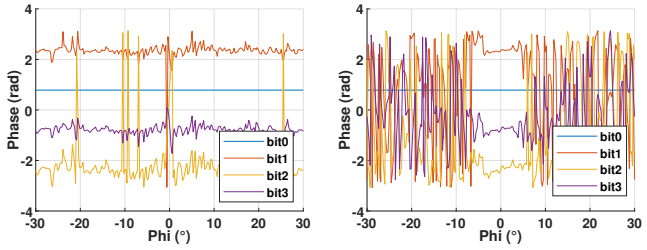

(a) $a_m = 1$. (b) $a_m = g(\varphi_m)$.

Figure 7: Phase encoding with 4 states in simulation.

channel (HH). We first divide the 2π phase circle uniformly by the total number of phase encoding states N_B, and manipulate the phase term of G_l in Eq. (7) as follows:

$$G_{v,l} = G_0, \quad G_{h,l}^{(b)} = G_0\, e^{j2\pi \frac{b}{N_B}}, \forall\, l. \tag{15}$$

Here, b denotes the b-th phase state. Eq. (15) aims to create a constant phase of $2\pi \frac{b}{N_B}$ of (HH/VV) over the specified angle regions. The simulated relative phase pattern in Fig. 7b shows multiple distinct phase states in the targeted region $\phi \in [-7.5°, 7.5°]$. Notably, if the phase-amplitude profile $g(\varphi_m)$ is set to be constant, large phase variations are observed at $0°$, causing design failure.

4 Radar Signal Processing for Road Sign Detection

Our signal processing pipeline builds upon a standard mmWave MIMO radar framework [34, 44], which we have extended to support quad-polarization channels. Furthermore, we incorporate custom algorithms specifically for detecting and decoding our polarimetric metasurface road signs.

4.1 A Primer on Polarimetric Radar Signal Processing

mmWave radar systems typically employ arrays of transmit (Tx) and receive (Rx) antennas to emit and capture multiple radar chirps. After ADC sampling, a multidimensional data cube is acquired and processed through the standard *Range–Doppler–Angle* pipeline. Range processing estimates target distance via FFTs (for FMCW radars) or correlations (for pulse- or Golay-based systems), isolating targets by their propagation delay. Subsequently, Doppler FFTs across chirps yield target velocity, and angular estimation on the antenna dimension determines the direction of arrival.

In our quad-polarimetric radar, these processing steps are performed independently for each of the four polarization channels (HH, HV, VH, and VV). For each target that can be resolved in range, angle, and velocity, a 2×2 polarimetric scattering matrix (Eq. (1)) is then estimated. Compared to a single-polarization radar, the quad-polarimetric design doubles sensing latency (due to Tx-H/V multiplexing) and quadruples computational complexity (due to 4-channel processing).

4.2 MetaPolar Sign Detection

MetaPolar's road sign detection is designed to integrate seamlessly into a standard radar signal processing pipeline. To efficiently identify candidate targets, we employ the Constant False Alarm Rate (CFAR) algorithm—an adaptive thresholding technique that maintains a consistent false alarm probability under varying noise and clutter conditions. Since MetaPolar road signs are stationary, Doppler processing is omitted, and we instead apply 1D CFAR detection directly to the range profiles generated in the early stage of the radar processing pipeline.

In a quad-channel polarimetric radar, CFAR is applied independently to each polarization channel–HH, HV, VH, and VV–yielding a list of range bins that exceed the local noise-adaptive detection threshold. These range bins represent potential targets. To classify a range bin as a MetaPolar tag candidate, we apply the following three criteria:

1. Cross-polarization detection: The bin must pass CFAR detection in either the HV or the VH channel.

2. Co-polarization detection: The bin must pass CFAR detection in both the HH and VV channels.

3. Polarization conversion ratio: The ratio of cross- to co-polarized power must exceed a predefined threshold.

Criterion 1 ensures that the candidate exhibits a strong cross-polarized reflection—an essential property of MetaPolar tags, which utilize polarization conversion for identification. While HV and VH channels are theoretically reciprocal in monostatic radar systems, hardware imperfections and spatial separation between antenna elements often result in slight mismatches. To simplify processing, we incoherently average the HV and VH magnitudes and apply CFAR to the resulting composite channel.

Criterion 2 ensures that sufficient SNR is available for decoding data embedded in the co-polarization channels. Due to possible

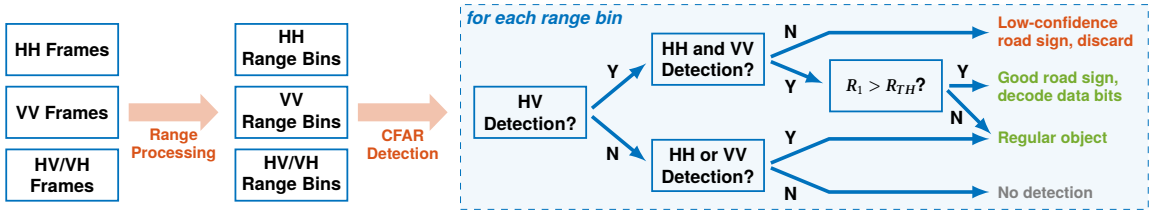

Figure 8: Signal processing working flow for MetaPolar road sign detection.

fabrication asymmetries or angular nulls in the metasurface beam pattern (Fig. 6), the co-polarized channels may experience attenuation at certain incidence angles. By requiring both HH and VV to pass, the detector remains robust under mild channel degradation.

Criterion 3 helps reject false positives caused by large environmental reflectors (*e.g.*, vehicles, poles). Although such reflectors exhibit weak polarization conversion, the large absolute RCS can still pass the CFAR detection for the HV/VH channel, leading to misdetection. To distinguish them from MetaPolar tags, Criterion 3 computes the polarization conversion ratio (PCR), defined as:

$$R_1 = \sqrt{\frac{S_{HV}^2 + S_{VH}^2}{S_{HH}^2 + S_{VV}^2}}, \tag{16}$$

where $S_{HH}, S_{HV}, S_{VH}, S_{VV}$ are the complex RCS at the range bin being examined.

If a range bin satisfies Criteria 1 and 3 but fails Criterion 2, it is marked as a MetaPolar tag without sufficient data for decoding. In this case, the tag may still serve as a fixed anchor for localization, as shown in prior work [36]. If Criterion 2 is satisfied but either Criterion 1 or 3 fails, the target is considered a regular reflector, and no MetaPolar-specific processing is applied. Standard radar post-processing continues as usual.

4.3 Sign Decoding and System Calibration

For the range bins that satisfy all three criteria, the co-polarization RCS ratio R_2 is computed to decode the data bits.

$$R_2 = S_{HH}/S_{VV}. \tag{17}$$

In practical automotive environments, the estimated RCS of the reflector can vary due to various factors such as interrogating angles, cluttering, and mobility. To mitigate this difficulty and improve decoding accuracy, we average the measurements across multiple pulses/chirps. Since the SNR of measurement samples can vary significantly (often exceeding 10 dB) and higher-SNR samples are more reliable, we employ a weighted averaging algorithm to prioritize such samples:

$$\bar{R}_1 = \sum w_1^{(i)} R_1^{(i)}, \quad \bar{R}_2 = \sum w_2^{(i)} R_2^{(i)}, \tag{18}$$

$$w_1^{(i)} = \sqrt{S_{HV}^2 + S_{VH}^2 + S_{HH}^2 + S_{VV}^2}, \quad w_2^{(i)} = \sqrt{S_{HH}^2 + S_{VV}^2}. \tag{19}$$

However, the true R_1 and R_2 values can not be known accurately from full-wave simulation due to fabrication tolerances. Moreover, different radar channels also have constant phase offsets due to hardware mismatches. Therefore, to decode the data, a one-time calibration must be conducted for each MetaPolar road sign. To do so, we place the metasurface road sign at the boresight of the radar and measure its RCS matrix. Multiple measurements at different ranges and orientations should be conducted to reduce the variation and achieve a reliable estimation of the true value R_{1-k} and R_{2-k}.

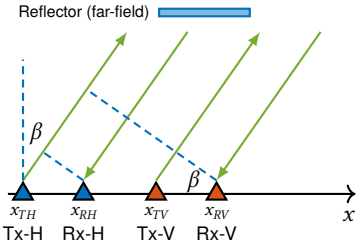

Figure 9: Illustration of the angle of arrival: extra phase shifts can be introduced.

With these calibrated reference values, the final data bits (p and q) are decoded from the weighted-average measurements ($\bar{R}_1$ and $\bar{R}_2$) by finding the symbols with the minimum Euclidean distance:

$$\begin{cases} p = \arg\min_k (\|\bar{R}_1 - R_{1-k}\|^2), \\ q = \arg\min_k (\|\bar{R}_2 - R_{2-k}\|^2). \end{cases} \tag{20}$$

4.4 Impact of the Angle of Arrival

In MIMO radar systems, the phase of the target is also related to the antenna location and the angle of arrival (AoA) of the target. If the antennas are placed on a single line as shown in Fig. 9, at locations x_{TH}, x_{RH}, x_{TV}, and x_{RV}, the extra phase shift between S_{HH} and S_{VV} caused by the AoA can be written as:

$$\Delta\psi = 2\pi \frac{\sin\beta}{\lambda}(x_{RV} - x_{TH} - x_{RH} + x_{TV}). \tag{21}$$

The AoA β needs to be estimated accurately (*e.g.* using MUSIC [28]) to compute $\Delta\psi$ and subsequently compensate S_{HH} or S_{VV}. For common 5G mmWave dual-polarization phased arrays [10, 11], the H-pol and V-pol antennas share the same location (*i.e.* $x_{TH} = x_{TV}$ and $x_{RH} = x_{RV}$), and therefore the estimated phase is not impacted by the AoA, and no compensation is required.

5 Implementation

5.1 Metasurfaces

We opt to employ a 2-layer FR-4 PCB design for both the SRR and the XD based metasurfaces, as shown in Fig. 10a. The SRR or XD patterns are printed on the top layer of the PCB. The bottom layer is fully covered with copper, serving as a ground plane. A solder mask layer covers the bottom layer as a protection layer. The total thickness of the PCB is around 0.6 mm and the FR-4 prepreg thickness is around 0.47 mm.

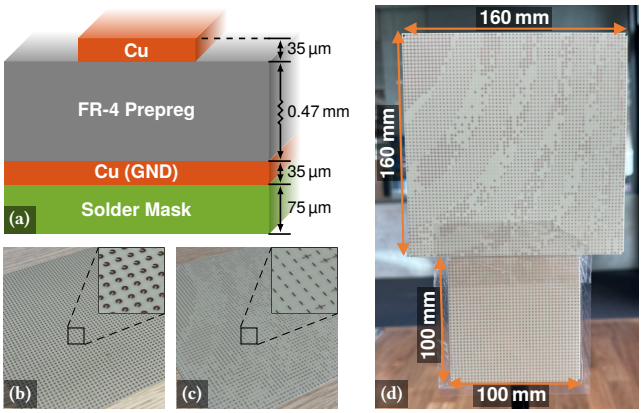

Figure 10: MetaPolar PCB implementation. (a) PCB layer stackup. (b) Polarization converter. (c) Anisotropic beamshaper. (d) Concatenation.

Table 3: Summary of designed metasurfaces.

	Dim.	$\phi_{\max}$	$\theta_{\max}$	α	$\angle G$	P	Q
XD-phase-0-H	64×64	10°	5°	−25 dB	0°	30	20
XD-phase-0-V	64×64	10°	5°	−25 dB	0°	30	20
XD-phase-1-H	64×64	10°	5°	−25 dB	0°	30	20
XD-phase-1-V	64×64	10°	5°	−25 dB	180°	30	20
SRR-amp-0	40×40	10°	5°	−25 dB	0°	25	15
SRR-amp-1	64×64	10°	5°	−25 dB	0°	30	20

At the design stage, we use ANSYS HFSS to perform full-wave simulations for the unit cells. The relative permittivity of the FR-4 material D_k is configured as 4.2 per the manufacturer's specification, and the loss tangent at the radar's center frequency (60 GHz) is estimated to be 0.02. To find the optimal dimension of the SRR, we perform a sweep of r, g, and w in simulation and select the set of dimensions that yields the highest polarization conversion ratio. The final dimension of the SRR used for fabrication is: $r = 0.6$ mm, $g = 0.4$ mm, $w = 0.4$ mm. To design the XD, we first fix the width $w = 0.2$ mm and then sweep the dipole length L_x and L_y in the simulation. The phase-length curve (Fig. 3c) and phase-amplitude (Fig. 3c) curve can be found subsequently.

We fabricate two polarization converters and two anisotropic beamshapers to create four amplitude-phase states: A0-P0, A0-P1, A1-P0, and A1-P1. Their design configuration is listed in Tab. 3.

The optimization framework in Sec. 3.3 and 3.4 is implemented through the optimization toolbox in Matlab, resulting in the optimized phase vectors. For SRRs, the phases are quantized to 1 bit to the closest phase (0 or 180°). We subsequently designed a Rust program to map the phase vectors to the shape of the unit cells and generate an image of the final metasurface by using PDF primitives. Lastly, the images are imported into Altium Designer, and PCB layouts are produced. The amortized cost for a single piece 64×64 metasurface is about 1.5 USD, and for 40×40 is less than 1 USD.

5.2 Polarimetric Radar Platform

We implement our polarimetric measurements on an enhanced version of the M^3 software-defined radio platform [43] operating at the 60 GHz band. The platform is equipped with four 8×8-antenna phased arrays with linearly polarized antennas. We place 2 phased arrays with the antenna polarization aligned with the horizontal line and 2 phased arrays rotated by 90°. This configuration yields the full scattering matrix $[S_{HH}, S_{HV}, S_{VH}, S_{VV}]$, as shown in Fig. 11b. To suppress direct-path leakage, arrays are spaced apart and interleaved with RF-absorbing foam. The phased array supports a 1-bit amplitude and a 2-bit phase beamformer; a codebook can be preloaded to enable real-time beamscanning. Each array supports 1-bit amplitude and 2-bit phase control via a preloaded DFT-based codebook, enabling real-time two-dimensional beam scanning [41].

Baseband processing is handled by an AMD RFSoC 4×2 evaluation board [27], which provides two DAC outputs and four ADC inputs, supporting 1 Tx channel and 2 Rx channels. To support 2 Tx channels, we split one DAC output into two transmit chains using a broadband splitter [21]. The transmitters operate in time-division multiplexing, while both receive channels remain continuously active. Four general-purpose I/O lines on the RFSoC synthesize synchronized control waveforms for the phased-array beamformer, ensuring each radar frame corresponds to a single beam direction. All polarimetric data capture and control logic are implemented in PYNQ, a Python-based FPGA framework for RFSoC platforms [3].

5.3 Radar Waveform

Following the principle of integrated communication and sensing, we extrapolate the radar range and angular profiles from the channel impulse response (CIR) between the transmit and receive antennas. We implement the 802.11ad/ay-like CIR estimation on RFSoC 4×2 [27] following a similar architecture in [14]. Two sets of 128-length Golay sequences G_a and G_b are used, and more specifically, the channel estimation field (CEF) is defined as [12]:

$$[-G_b, -G_a, G_b, -G_a, -G_b, G_a, -G_b, -G_a, -G_b], \tag{22}$$

with a total sequence length 128×9. Due to the perfect correlation property of the Golay complementary sequence [7, 17], the CIR can be efficiently estimated by performing cross-correlation between the known CEF sequence and the received ADC samples on FPGA.

The sampling frequency for all the ADC and DAC channels is $f_s = 1.966$ Gsps, and the resulting time-of-flight (ToF) resolution is $\Delta\tau = 1/f_s = 0.51$ ns. For monostatic radar sensing, the range resolution $d_{res} = c\,\Delta\tau/2 = 76.3$ mm. Such a high range resolution ensures better distinction between reflectors at a close range, ensuring robustness in a practical clutter-rich environment.

6 Evaluation

6.1 Effectiveness of the Polarization Converter

To evaluate the performance of the SRR-based polarization converter, we fabricate two metasurfaces, one with an identical SRR pattern and the other with the designed semi-retroreflective pattern, both with 64×64 unit cells. We place the metasurface 5 m away in front of the polarimetric radar, and use a laser leveler to align their relative orientation.

We first measure the metasurface with identical SRR unit cells. We rotate the metasurface around the Z-axis (Fig. 4b) from 0°to 45° and measure the polarization conversion ratio. Fig. 12a shows that the conversion ratio reaches a maximum of 17 dB at $\alpha = 45°$, which is aligned with the simulation. The experiment verifies the design

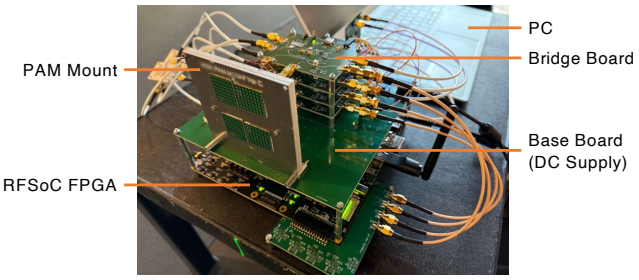

(a) SDR platform. (b) Phased array layout. (c) Experiment setup.

Figure 11: The quad-channel polarimetric software radio platform.

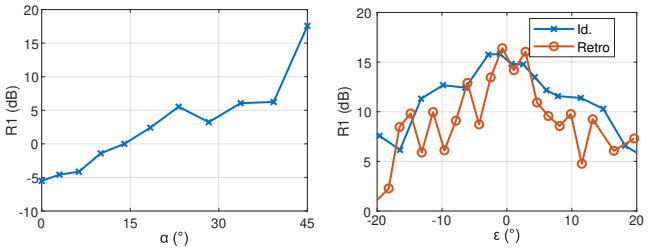

(a) Conversion ratio. (b) Orientation error tolerance.

Figure 12: Polarization conversion.

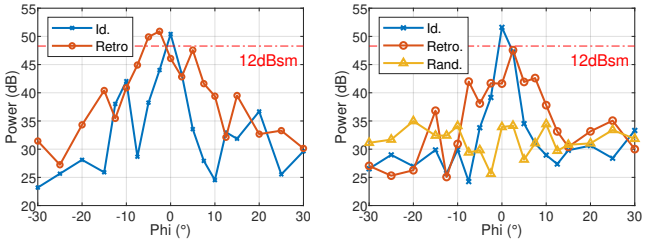

(a) Split ring resonator (SRR). (b) Crossed dipole (XD).

Figure 13: The retro-reflective beam pattern.

of the SRR-based metasurface for maximization of polarization conversion.

Next, we measure the effect of orientation misalignment between the radar phased array and the designed retroreflective metasurface. Fig. 12b shows the impact when rotating the metasurface from -20° to 20°. Unlike the aforementioned metasurface with identical SRRs, the retro-reflective metasurface exhibits a non-smooth polarization conversion ratio degradation over ϵ. This is caused by the irregular beam shape from the co-polarization component, as the HH and VV reflection phase varies randomly between 0° and 180° (Sec. 3.2.1) in the presence of orientation error. Despite the practical artifact, a polarization conversion ratio above 10 dB is maintained even with a 10°misalignment, demonstrating the robustness of the polarization converter.

6.2 Semi-Retroreflective Beam Pattern

We then validate the effectiveness of the designed semi-retroreflective beam pattern (Sec. 6.2). Both the SRR metasurface and the cross-dipole metasurface are designed to maximize reflection at a range of $-7.5^\circ < \phi < 7.5^\circ$ and $-5^\circ < \theta < 5^\circ$. For reference, we also fabricate and measure the metasurface with identical unit cells and with random unit cell patterns. In addition, a corner reflector with an RCS = 12 dBsm is also measured.

We put the metasurface at the foresight of the radar at a distance of 5 m and rotate the metasurface along the Y-axis (Fig. 4b) from -30° to 30°. Fig. 13 shows the measured retro-reflective pattern for both SRR and XD. The metasurfaces with identical patterns exhibit a sharp peak at 0 degrees due to their specular reflective property, and drop by around 17 dB at $\pm5^\circ$. They are unsuitable as a road sign due to the highly constrained readable angle. While the metasurface with random unit cells exhibits a wide retro-reflective range, the overall reflection gain is low and fluctuates randomly. This greatly limits the readable range and undermines the robustness of the amplitude encoding. In contrast, the retro-reflective metasurface demonstrates a flatter and higher gain within the designed region ($-7.5^\circ < \phi < 7.5^\circ$). The XD metasurface achieves an average RCS of 6.80 dBsm, 11.89 dB higher than the random metasurface. The SRR metasurface exhibits a higher reflective gain (RCS = 10.31 dBsm) than the XD metasurface because of XD's larger unit-cell attenuation, as discussed in Sec. 3.2.2. *The experiments verify the necessity and the effectiveness of the retro-reflective beam pattern design.*

At a 10 m distance, a $\pm7.5^\circ$ angular range corresponds to a lateral coverage of approximately 2.6 m—adequate for vehicle detection and communication in typical traffic settings. Moreover, as road signs are generally oriented toward oncoming vehicles, the designed semi-retroreflective pattern provides an effective balance between angular coverage and reflection gain, ensuring robust and efficient performance in real-world deployments.

6.3 Amplitude Encoding

As mentioned in Sec. 3.4.1 and 5.1, we fabricate two SRR metasurfaces of size 64×64 and 40×40 to create 2 amplitude encoding states.

In the first experiment, we place a single SRR metasurface at a range of 5 m, rotate the metasurface with $-10^\circ < \phi < -10^\circ$, and measure the corresponding reflection signal strength. The amplitude pattern in Fig. 14a shows that the 64×64 metasurface has a consistently larger reflection strength than the 40×40 one over the designed angles, with an average power difference of 6.0 dB.

In the second experiment, the SRR metasurfaces are concatenated with the same XD metasurface. We place the concatenated metasurface at a range from 4 m to 5 m and randomly vary the angle

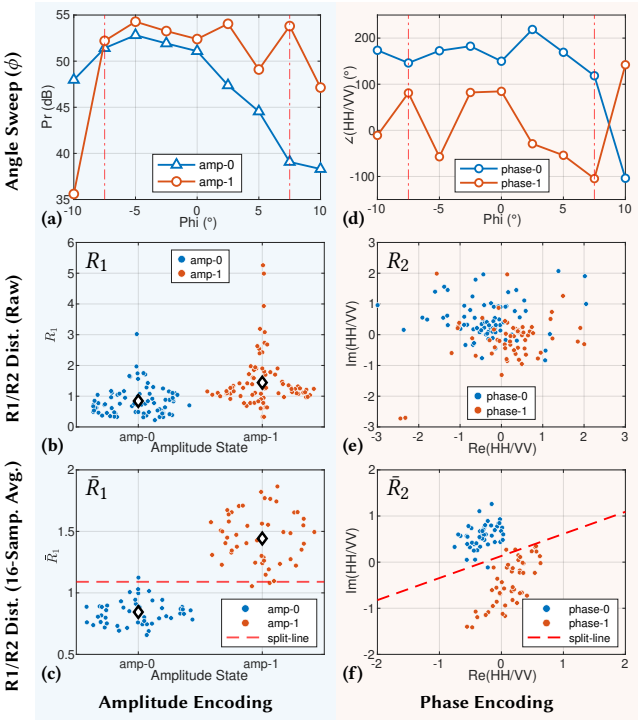

Figure 14: Amplitude and phase encoding. (a)–(c) Amplitude encoding. (d)–(f) Phase encoding.

ϕ by ±5 degrees and θ by ±3 degrees; and for each metasurface, 50 samples are collected. We select the corresponding range bins and calculate R_1 in Eq. (16) and plot the distribution in Fig. 14b. The mean values of R_1 are 1.47 and 0.82, which indicates a distinguishable difference. From previous evaluations regarding the retro-reflective patterns (Fig. 13), we see random fluctuation of the Cross- and Co-polarization reflection strength over angles. As the R_1 value is computed using the ratio of two, we also observe a high variance. Nonetheless, with the weighted averaging method, the variance can be lowered significantly. As shown in Fig. 14c, a threshold at $R_1 = 1.09$ can correctly classify 97% of the samples. Detailed evaluation of decoding performance will be discussed in Sec. 4.3. *The results indicate that by concatenating different polarization converters with the anisotropic beamshaper, two distinguishable amplitude states can be created.*

6.4 Phase Encoding

Here we evaluate two anisotropic beamshapers (XD-phase-0 and XD-phase-1 in Tab. 3) with different phase encoding (separated by π). Similar to the prior setup, we first put them at a range of 5 m, rotate the metasurface from $-10° < \phi < -10°$, and measure the reflection signal. The corresponding range bin is selected, and the phase of HH/VV is extracted. Fig. 14d shows that XD-phase-0 and XD-phase-1 exhibit separated phase patterns over the designed angle range ($-7.5° < \phi < 7.5°$), with a minimum phase separation of 65.4°. XD-phase-0 exhibits smaller variation because the H-dipole pattern and the V-dipole pattern are identical (Tab. 3); even if the actual retro-reflective patterns deviate from simulation, the impact is cancelled out through the division of HH/VV. On the contrary, the H and V dipole patterns on XD-phase-1 are optimized independently based on different optimization goals (Eq. (15)). Although the ideal phase difference should be constant, in practice, the amplitude-phase mapping $g(\varphi)$ in Eq. (9) cannot be estimated accurately, resulting in high variation in the relative phase pattern.

Next, we concatenate the XD-phase-0/1 metasurface with a 64×64 SRR polarization converter, and put them 4 m to 5 m away from the radar. We change the angle ϕ by ±5° and θ by ±3°, and collect 50 samples for each metasurface. Fig. 14e shows the distribution of R_2 = HH/VV, which exhibits two clusters on the complex plane, following a similar pattern as the constellation of classical Binary Phase-Shift Keying modulation. Due to the small millimeter-level wavelength, the phase variations are inevitable. Nonetheless, the variations can be reduced by performing multi-sample weighted averaging (Sec. 4.3) for samples captured at slightly different locations or angles. Fig. 14f shows that even with 16-sample averaging, the clusters become much more concentrated and a single line can easily divide the clusters with < 3% error. *The result shows the effectiveness of the phase encoding design and its robustness over different angles and ranges.*

6.5 Road Sign Detection

To evaluate MetaPolar 's ability to distinguish road signs from typical roadside objects, we tested four representative target classes:

- **Specular reflector:** metal board (21.6 cm × 27.9 cm), always oriented face-on to the radar;
- **Diffuse scatterer:** a 1.7 m tall pedestrian, sampled with front, back, and side orientations;
- **Artificial retroreflector:** trihedral corner reflector (12 dBsm), placed at random poses;
- **MetaPolar tag:** same dataset as Secs. 6.3–6.4, collected at 4–5 m range and within ±5° azimuth, ±3° elevation (50 samples per sign).

All non-tag objects were measured at random ranges between 3–8 m. Detection follows the CFAR-based pipeline in Fig. 8, with amplitude threshold $R1_{\text{th}} = 0.2$ (Sec. 2). As shown in Fig. 15a, regular objects produce zero false alarms for $P_{\text{fa}} < 10^{-3}$. MetaPolar signs achieve single-capture detection rates of 78–90% depending on P_{fa}, and with majority voting over 5–7 slightly varied captures, detection exceeds 99% (Fig. 15c). These results demonstrate robust discrimination of MetaPolar tags from common clutter.

6.6 Road Sign Decoding

We next quantify bit-level decoding performance for all detected MetaPolar signs. Due to peak spreading, each of the four tag categories (A0-P0, A0-P1, A1-P0, A1-P1) yielded 69–84 detections from the 50 raw samples. For $N_{\text{samp}} = 1$–29, we randomly draw that many samples, apply the weighted-averaging decoder (Sec. 4.3), and repeat 100 trials per N_{samp}. Single-capture accuracy is only ≈ 55% for four-way classification. As Fig. 15c shows, multi-sample averaging rapidly improves performance: amplitude decoding (R_1) exceeds 90% at 15 samples, phase decoding (R_2) at 7 samples, and overall accuracy surpasses 99% at ≈ 30 samples. At a 10 ms radar frame rate [35], 30 frames (300 ms) correspond to about 5 m of travel at 40 mph, a practical latency for automotive use. We therefore adopt $N_{\text{samp}} = 16$ for all subsequent experiments. *These findings*

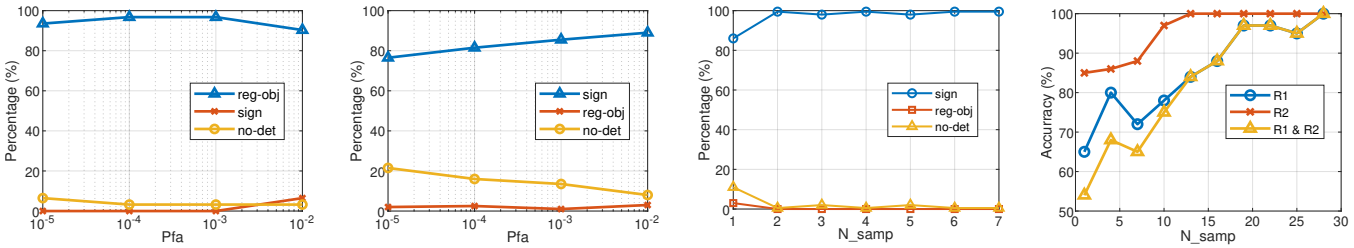

(a) Regular objects detection. (b) Sign detection. (c) Sign detection (pfa=1e-3). (d) Sign decoding.

Figure 15: Sign detection and decoding results. (a) and (b) show the results with one capture, while (c) and (d) use multiple samples to enhance the performance.

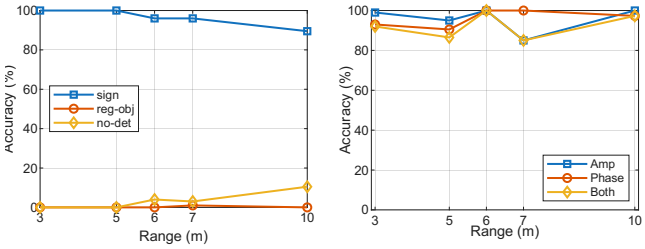

(a) Detection (pfa=1e-3, n_samp=16) (b) Decoding (16-sample avg.)

Figure 16: Impact of the distance. (a) Sign detection accuracy. (b) Sign decoding accuracy.

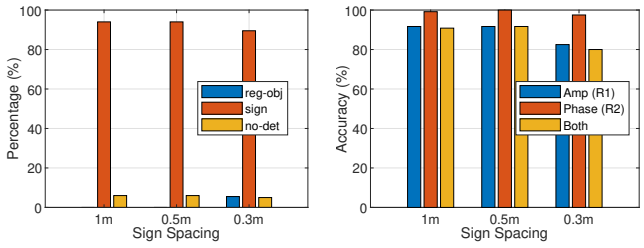

(a) Detection (pfa=1e-3, n_samp=16). (b) Decoding (16-sample avg.).

Figure 17: Detection and decoding performance of two tags with different spacing.

confirm reliable 1-bit amplitude and 1-bit phase decoding in realistic V2I scenarios.

6.7 Impact of Distance

The reliability of radar-based MetaPolar detection and decoding hinges on the received SNR, which follows the classic radar equation [31]:

$$\mathrm{SNR} = \frac{\sigma P_t G_{ant}^2 G_{tx} G_{rx} \lambda^2}{(4\pi)^3 d^4 P_n}, \tag{23}$$

where σ is the tag's RCS (Sec. 6.2), P_t the transmit power, G_{ant}, G_{tx}, and G_{rx} the antenna and array gains, $\lambda = 5$ mm the wavelength, d the range, and P_n the receiver noise power. The detection range primarily depends on radar hardware and waveform parameters, while MetaPolar's design only affects σ, measured as 6.80 dBsm in Sec. 6.2. As a reference, a typical pedestrian exhibits an RCS of about −6 dBsm at mmWave frequencies [40].

We evaluate MetaPolar tags at distances from 3 m to 10 m using our custom radar platform. As the path loss increases with range, we adjust P_t respectively to maintain a constant SNR. At each range, two tags are randomly selected, and 30 measurements are collected per tag over horizontal angles $\phi \in [-5°, 5°]$ and vertical $\theta \in [-3°, 3°]$, then the same CFAR thresholds and calibration are applied as in Sec. 6.6.

Figure 16 shows a slight decline in detection rate with range, despite constant theoretical SNR. This arises from the radar front end's limited dynamic range: higher P_t amplifies Tx–Rx leakage, pushing the receiver amplifier toward gain compression. In addition, the increased power of multipath and clutter lowers the effective echo SNR, causing more missed and false detections. Nevertheless, the decoding accuracy remains stable across all tested distances, as the detection step inherently filters out low-SNR samples, ensuring that only high-confidence echoes are passed to the polarimetric decoding pipeline.

6.8 Scaling Encoding Capacity and Resolving Multiple Road Signs

Although a single MetaPolar tag can only reliably encode 2 bits of information, multiple tags can be deployed in close proximity, forming a tag array to increase the encoding capacity. To evaluate this scalability, we position one tag at 7 m away from the radar, and additional tags at 6 m, 6.5 m, and 6.7 m, respectively, corresponding to a decreasing spacing (1 m, 0.5 m and 0.3 m) from the reference tag. Notably, the radar's range resolution is 76.3 mm (Sec. 5.3), which is smaller than the tags' spacing. All tags are positioned slightly off the radar's boresight–*i.e.*, offset from the centerline perpendicular to the phased arrays–to avoid direct line-of-sight occlusion and to emulate realistic drive-by scenarios, where a vehicle approaches the tag array at a shallow angle.

We measure two combination of MetaPolar tags: (A0-P0 + A0-P1) and (A1-P0 + A1-P1), vary the orientation of the tags ($\phi \in [-5°, 5°]$ and $\theta \in [-3°, 3°]$) and capture 30 samples for each combination. Fig. 17a shows the sign detection result with pfa=1e-3. The detection rate remains approximately unchanged compared with the single sign case (Fig. 16a) for 1 m and 0.5 m spacing, yet it decreases as the spacing reduces to 0.3 m. While targets separated by more than the radar's nominal range resolution are theoretically distinguishable, in practice, spectral leakage causes energy from one range bin to spill into adjacent bins. In our experiments, the signal

Table 4: Comparison of mmWave radar-readable tags.

	MetaPolar	RoS [22]	UniScatter [26]	Millimetro [32]	Omniscatter [4]
Frequency Band	60 GHz	77 GHz	28–77 GHz	24 GHz	24/60 GHz
Retroreflector	2D Unit-Cell Array	Van Atta Array	Luneburg Lens	Van Atta Array	Van Atta Array
Capacity	2 bits/unit	4 bits	100 bits/s	1100 bits/s	12 bits/s
Reading Angle	$-7.5° \sim 7.5°$	$-60° \sim 60°$ †	$-35° \sim 35°$	$-30° \sim 30°$	$-90° \sim 90°$
Reading Range	> 10 m	< 6 m	30 m	> 100 m	40/4 m @ 24/60 GHz
Multiple Tags	Yes	No	Yes	Yes	Yes
Power	0	0	100 mW	3 µW	7 µW @ 24 GHz
Cost	$3	> $500	$400	> $500	> $3,000 @ 60 GHz

† Requires continuous radar scanning over the whole angle range.

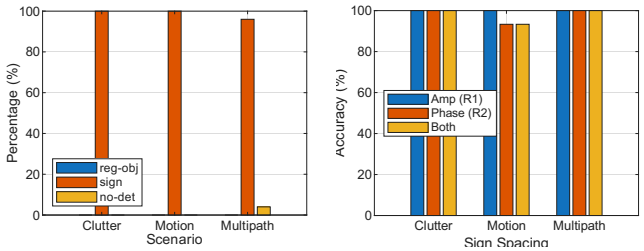

(a) Detection (pfa=1e-3, n_samp=16). **(b) Decoding (16-sample avg.).**

Figure 18: Performance of tag detection and decoding in a complex environment.

peak from one tag was occasionally 10–20,dB stronger than that of a neighboring tag. This power disparity allows the sidelobes of the stronger signal to mask the weaker one, resulting in missed detections. Empirically, we observe that when the spacing between two tags exceeds 4× the range resolution, mutual interference becomes negligible, enabling reliable and independent detection. Once the tags are detected, our polarimetric decoding pipeline is applied to each individually, achieving accuracy comparable to the single-tag case (Fig. 17b).

A single MetaPolar tag encodes 2 bits; deploying multiple tags with a minimum spacing of ∼ 4× the range resolution (0.3 m) enables linear capacity scaling. For instance, four tags encode 8 bits (256 symbols), supporting diverse traffic instructions (*e.g.*, stop, yield, pedestrian crossing). Such configurations are practical in roadside settings, where tags can be placed at distinct ranges or mounted on separate poles.

6.9 Performance in Multipath, Cluttering and Dynamic Environment

To evaluate MetaPolar under realistic automotive radar conditions, we conduct experiments in environments containing multipath, clutter, and dynamic reflectors. A MetaPolar sign is placed near environmental reflectors with range separations between 0.5 m and 3 m, and three representative scenarios are tested:

(1) Stationary clutter: a tree serves as a nearby reflector, with its relative position to the road sign varied for each sample.
(2) Moving objects: a walking human moves randomly around the sign with varying direction and velocity (0–2.5 m/s).
(3) Multipath environment: an indoor, reflection-rich setting where the MetaPolar sign is placed at a random location.

In all cases, the radar faces the metasurface from a distance of 6 m. One MetaPolar sign is selected and measured 20 times. As shown in Fig. 18, MetaPolar maintains a high detection accuracy exceeding 95%, with only occasional missed detections. Decoding performance remains comparable to that observed in the controlled setting (Sec. 6.6). The wide bandwidth of the mmWave radar enables fine delay resolution, effectively separating reflections with similar time-of-flight and mitigating multipath interference. *These results demonstrate that MetaPolar offers robust detection and decoding performance even in cluttered or dynamic real-world environments.*

7 Related Works

mmWave backscattering tags. mmWave backscattering has been widely explored for joint radar–communication systems. Prior work [4, 5, 20, 24, 32] predominantly builds on Van Atta array designs to achieve wide angular coverage, combined with RF switches for information modulation. These systems can achieve centimeter-level localization accuracy and support simultaneous multi-tag decoding. For instance, OmniScatter [4] builds on a Van Atta array with RF switches for FSK modulation, whereas UniScatter [26] adopts a distinct design based on a Luneburg lens and graphene surface to enable wideband (24 GHz to 77 GHz) backscattering.

However, these designs rely on active RF components and require external power (typically on the order of 10 mW). In addition, Van Atta arrays incur higher fabrication costs due to high-frequency PCB requirements and specialized substrates. In contrast, MetaPolar is fully passive and enables polarimetric encoding using low-cost, low-profile PCBs, significantly reducing both deployment complexity and fabrication cost.

mmWave passive metasurface. Passive metasurfaces have recently gained traction for enhancing mmWave coverage and augmenting radar sensing. Prior work explores diverse fabrication approaches, including 3D-printed designs [25], paper-based implementations [19, 29], and PCB-based metasurfaces [23], often focusing on beam shaping and signal focusing. Beyond communications, metasurfaces have also been used as radar landmarks for drone navigation and localization [13, 15], as well as for enabling non-line-of-sight sensing in automotive scenarios [38]. While these systems share similar unit-cell structures, MetaPolar introduces a fundamentally different paradigm by encoding information in the polarimetric response of the metasurface.

The most closely related work is RoS [22], which encodes bits in the spatial RCS profile. RoS requires lateral observation and multiple temporal measurements as the vehicle moves past the sign

to recover spatial variations. In contrast, MetaPolar encodes information in the polarimetric RCS, enabling single-shot decoding from a fixed viewpoint. This design improves detection range, removes motion dependency, and reduces decoding latency. Table 4 summarizes these differences.

Polarization and anisotropic metasurface. Recent studies have extensively explored polarization manipulation using electromagnetic metasurfaces [30]. A variety of anisotropic converters and multi-resonant structures have been explored for cross-polarization control, including I-shaped [18], H-shaped [39], twisted SRR [9], and double-head arrow [8, 33]. A double-layered crossed dipole structure is also proposed in [37] to create dual-polarized reflection patterns. In contrast, MetaPolar is the first work to employ polarization conversion and anisotropic metasurfaces to encode information specifically for radar reading.

8 Discussion

8.1 Availability of Quad-Polarized Radars

Although quad-polarized radars are not yet widely deployed in commercial automotive systems, polarization diversity is already prevalent in mmWave communication hardware. Dual-polarized phased arrays are standard in modern 5G systems [1, 10, 11] and are expected to remain integral to emerging 6G integrated sensing and communication (ISAC) architectures. As V2X platforms evolve, the polarization channels inherent in such systems can be naturally leveraged for joint radar–communication functionality. In this context, MetaPolar offers a scalable and hardware-compatible solution for V2I communication without requiring additional RF front-end modifications.

8.2 Increasing Per-Unit Encoding Capacity

The primary challenge in increasing per-tag encoding capacity is not SNR, but the robust discrimination of encoded states under varying incident angles. Since the metasurface response results from the coherent superposition of reflections across all unit cells, small fabrication tolerances and material inhomogeneities can distort the intended complex reflection profile (Fig. 7). Future work may focus on improving the modeling accuracy of lossy dielectrics (Fig. 3d) or exploring alternative metasurface structures [30] to further increase capacity.

9 Conclusion

We have introduced MetaPolar, a fully passive mmWave metasurface tag that encodes information in the polarimetric RCS matrix and can be read reliably by standard automotive radars. Fabricated on low-cost PCBs, MetaPolar demonstrates scalable encoding, multi-tag simultaneous reading, and resilience to environmental clutter. These results underscore the potential of polarimetric metasurfaces for cost-effective, scalable I2V communication in next-generation intelligent transportation networks.

Acknowledgments

We appreciate the insightful comments and feedback from the anonymous reviewers and shepherd. The work reported in this paper is supported in part by the NSF under Grants CNS-2403124, CNS-2408393, CNS-2346550, and CNS-2312715.

References

[1] 5G Americas. 2020. Understanding mmWave Spectrum for 5G Networks. Retrieved July 1, 2025 from https://www.5gamericas.org/wp-content/uploads/2020/12/InDesign-Understanding-mmWave-for-5G-Networks.pdf

[2] The 5G Automotive Association (5GAA). 2024. A visionary roadmap for advanced driving use cases, connectivity, and technologies. Retrieved July 1, 2025 from https://5gaa.org/content/uploads/2025/01/5gaa-roadmap-iii-wp.pdf

[3] AMD. 2024. *PYNQ | Python Productivity to AMD Adaptive Compute platforms.* AMD. Retrieved July 1, 2025 from https://www.pynq.io

[4] Kang Min Bae, Namjo Ahn, Yoon Chae, Parth Pathak, Sung-Min Sohn, and Song Min Kim. 2022. OmniScatter: extreme sensitivity mmWave backscattering using commodity FMCW radar. In *Proceedings of the 20th Annual International Conference on Mobile Systems, Applications and Services* (Portland, Oregon) *(MobiSys '22)*. Association for Computing Machinery, New York, NY, USA, 316–329. https://doi.org/10.1145/3498361.3538924

[5] Kang Min Bae, Hankyeol Moon, Sung-Min Sohn, and Song Min Kim. 2023. Hawkeye: Hectometer-range Subcentimeter Localization for Large-scale mmWave Backscatter. In *Proceedings of the 21st Annual International Conference on Mobile Systems, Applications and Services* (Helsinki, Finland) *(MobiSys '23)*. Association for Computing Machinery, New York, NY, USA, 303–316. https://doi.org/10.1145/3581791.3596869

[6] Geoff Boeing. 2020. A multi-scale analysis of 27,000 urban street networks: Every US city, town, urbanized area, and Zillow neighborhood. *Environment and Planning B: Urban Analytics and City Science* 47, 4 (2020), 590–608.

[7] SZ Budišin. 1991. Efficient pulse compressor for Golay complementary sequences. *Electronics Letters* 27, 3 (1991), 219–220. https://doi.org/10.1049/el:19910142

[8] Hongya Chen, Hua Ma, Jiafu Wang, Shaobo Qu, Yongqiang Pang, Mingbao Yan, and Yongfeng Li. 2016. Ultra-wideband transparent 90° polarization conversion metasurfaces. *Applied Physics A* 122 (2016), 1–5.

[9] Yongzhi Cheng, Yan Nie, Xian Wang, and Rongzhou Gong. 2013. An ultrathin transparent metamaterial polarization transformer based on a twist-split-ring resonator. *Applied Physics A* 111 (2013), 209–215.

[10] Jeremy Dunworth, Bon-Hyun Ku, Yu-Chin Ou, David Lu, Paul Mouat, Aliakbar Homayoun, Kaushik Chakraborty, Andrew Arnett, Gang Liu, Tony Segoria, et al. 2018. 28GHz phased array transceiver in 28nm bulk CMOS for 5G prototype user equipment and base stations. In *2018 IEEE/MTT-S International Microwave Symposium-IMS*. IEEE, New York, NY, USA, 1330–1333. https://doi.org/10.1109/MWSYM.2018.8439517

[11] Xiaoxiong Gu, Duixian Liu, Christian Baks, Ola Tageman, Bodhisatwa Sadhu, Joakim Hallin, Leonard Rexberg, Pritish Parida, Young Kwark, and Alberto Valdes-Garcia. 2019. Development, implementation, and characterization of a 64-element dual-polarized phased-array antenna module for 28-GHz high-speed data communications. *IEEE Transactions on Microwave Theory and Techniques* 67, 7 (2019), 2975–2984. https://doi.org/10.1109/TMTT.2019.2912819

[12] IEEE. 2012. IEEE Standard for Information technology – Telecommunications and information exchange between systems – Local and metropolitan area networks – Specific requirements – Part 11: Wireless LAN Medium Access Control (MAC) and Physical Layer (PHY) Specifications – Amendment 3: Enhancements for Very High Throughput in the 60 GHz Band. https://doi.org/10.1109/IEEESTD.2012.6168026

[13] Tatsuya Iizuka, Takuya Sasatani, Toru Nakamura, Naoko Kosaka, Masaki Hisada, and Yoshihiro Kawahara. 2023. MilliSign: mmWave-Based Passive Signs for Guiding UAVs in Poor Visibility Conditions. In *Proceedings of the 29th Annual International Conference on Mobile Computing and Networking* (Madrid, Spain) *(MobiCom '23)*. Association for Computing Machinery, New York, NY, USA, Article 50, 15 pages. https://doi.org/10.1145/3570361.3613264

[14] Jesus O. Lacruz, Rafael Ruiz Ortiz, and Joerg Widmer. 2021. A real-time experimentation platform for sub-6 GHz and millimeter-wave MIMO systems. In *Proceedings of the 19th Annual International Conference on Mobile Systems, Applications, and Services* (Virtual Event, Wisconsin) *(MobiSys '21)*. Association for Computing Machinery, New York, NY, USA, 427–439. https://doi.org/10.1145/3458864.3466868

[15] Maisy Lam, Laura Dodds, Aline Eid, Jimmy Hester, and Fadel Adib. 2023. 3D Self-Localization of Drones using a Single Millimeter-Wave Anchor. arXiv:2310.08778 [cs.RO] https://arxiv.org/abs/2310.08778

[16] Jong-Sen Lee and Eric Pottier. 2017. *Polarimetric Radar Imaging: From Basics to Applications.* CRC Press, Boca Raton, Florida, USA. https://doi.org/10.1201/9781420054989

[17] Wei-Chang Liu, Fu-Chun Yeh, Ting-Chen Wei, Ching-Da Chan, and Shyh-Jye Jou. 2013. A digital Golay-MPIC time domain equalizer for SC/OFDM dual-modes at 60 GHz band. *IEEE Transactions on Circuits and Systems I: Regular Papers* 60, 10 (2013), 2730–2739. https://doi.org/10.1109/TCSI.2013.2244321

[18] Hui Feng Ma, Gui Zhen Wang, Gu Sheng Kong, and Tie Jun Cui. 2015. Independent Controls of Differently-Polarized Reflected Waves by Anisotropic Metasurfaces. *Scientific Reports* 5, 1 (2015), 9605. https://doi.org/10.1038/srep09605

[19] Ruichun Ma, Shicheng Zheng, Hao Pan, Lili Qiu, Xingyu Chen, Liangyu Liu, Yihong Liu, Wenjun Hu, and Ju Ren. 2024. AutoMS: Automated Service for

mmWave Coverage Optimization using Low-cost Metasurfaces. In *Proceedings of the 30th Annual International Conference on Mobile Computing and Networking* (Washington D.C., DC, USA) *(ACM MobiCom '24)*. Association for Computing Machinery, New York, NY, USA, 62–76. https://doi.org/10.1145/3636534.3649347

[20] Mohammad Hossein Mazaheri, Alex Chen, and Omid Abari. 2021. mmTag: a millimeter wave backscatter network. In *Proceedings of the 2021 ACM SIGCOMM 2021 Conference* (Virtual Event, USA) *(SIGCOMM '21)*. Association for Computing Machinery, New York, NY, USA, 463–474. https://doi.org/10.1145/3452296.3472917

[21] Mini-Circuits. 2019. *ZFRSC-42-S+: 2 Ways Resistive Power Splitter, DC - 4200 MHz, 50Ω*. Mini-Circuits. Retrieved July 1, 2025 from https://www.minicircuits.com/pdfs/ZFRSC-42+.pdf

[22] John Nolan, Kun Qian, and Xinyu Zhang. 2021. RoS: passive smart surface for roadside-to-vehicle communication. In *Proceedings of the 2021 ACM SIGCOMM 2021 Conference* (Virtual Event, USA) *(SIGCOMM '21)*. Association for Computing Machinery, New York, NY, USA, 165–178. https://doi.org/10.1145/3452296.3472896

[23] John Nolan and Xinyu Zhang. 2025. Ricochet: Scalable Passive Beamforming for mmWave Networks Using Reflectarrays. In *IEEE INFOCOM 2025-IEEE Conference on Computer Communications*. IEEE, New York, NY, USA, 1–10.

[24] Ryu Okubo, Luke Jacobs, Jinhua Wang, Steven Bowers, and Elahe Soltanaghai. 2024. Integrated Two-way Radar Backscatter Communication and Sensing with Low-power IoT Tags. In *Proceedings of the ACM SIGCOMM 2024 Conference* (Sydney, NSW, Australia) *(SIGCOMM '24)*. Association for Computing Machinery, New York, NY, USA, 327–339. https://doi.org/10.1145/3651890.3672226

[25] Kun Qian, Lulu Yao, Xinyu Zhang, and Tse Nga Ng. 2022. MilliMirror: 3D printed reflecting surface for millimeter-wave coverage expansion. In *Proceedings of the 28th Annual International Conference on Mobile Computing And Networking* (Sydney, NSW, Australia) *(MobiCom '22)*. Association for Computing Machinery, New York, NY, USA, 15–28. https://doi.org/10.1145/3495243.3517024

[26] Kun Qian, Lulu Yao, Kai Zheng, Xinyu Zhang, and Tse Nga Ng. 2023. UniScatter: a Metamaterial Backscatter Tag for Wideband Joint Communication and Radar Sensing. In *Proceedings of the 29th Annual International Conference on Mobile Computing and Networking* (Madrid, Spain) *(MobiCom '23)*. Association for Computing Machinery, New York, NY, USA, Article 21, 16 pages. https://doi.org/10.1145/3570361.3592526

[27] Real Digital. 2021. *RFSoC 4x2 Kit*. AMD. Retrieved July 1, 2025 from https://www.amd.com/en/corporate/university-program/aup-boards/rfsoc4x2.html

[28] Ralph Schmidt. 1986. Multiple emitter location and signal parameter estimation. *IEEE Transactions on Antennas and Propagation* 34, 3 (1986), 276–280. https://doi.org/10.1109/TAP.1986.1143830

[29] Zhambyl Shaikhanov, Fahid Hassan, Hichem Guerboukha, Daniel Mittleman, and Edward Knightly. 2022. Metasurface-in-the-Middle Attack: From Theory to Experiment. In *Proceedings of the 15th ACM Conference on Security and Privacy in Wireless and Mobile Networks* (San Antonio, TX, USA) *(WiSec '22)*. Association for Computing Machinery, New York, NY, USA, 257–267. https://doi.org/10.1145/3507657.3528549

[30] Linda Shao and Weiren Zhu. 2024. Recent Advances in Electromagnetic Metamaterials and Metasurfaces for Polarization Manipulation. *Journal of Physics D: Applied Physics* 57, 34, Article 343001 (2024), 16 pages. https://doi.org/10.1088/1361-6463/ad4cfa

[31] Merrill Ivan Skolnik et al. 1980. *Introduction to Radar Systems*. Vol. 3. McGraw-Hill, New York, NY, USA.

[32] Elahe Soltanaghaei, Akarsh Prabhakara, Artur Balanuta, Matthew Anderson, Jan M. Rabaey, Swarun Kumar, and Anthony Rowe. 2021. Millimetro: mmWave retro-reflective tags for accurate, long range localization. In *Proceedings of the 27th Annual International Conference on Mobile Computing and Networking* (New Orleans, Louisiana) *(MobiCom '21)*. Association for Computing Machinery, New York, NY, USA, 69–82. https://doi.org/10.1145/3447993.3448627

[33] Hengyi Sun, Changqing Gu, Xinlei Chen, Zhuo Li, Liangliang Liu, and Ferran Martín. 2017. Ultra-wideband and broad-angle linear polarization conversion metasurface. *Journal of Applied Physics* 121, 17, Article 174902 (2017), 6 pages. https://doi.org/10.1063/1.4982916

[34] Texas Instruments. 2020. The Fundamentals of Millimeter Wave Radar Sensors. Retrieved July 1, 2025 from https://www.ti.com/lit/wp/spyy005a/spyy005a.pdf White Paper SPYY005A, Revision A.

[35] Texas Instruments. 2020. Programming Chirp Parameters in TI Radar Devices. Retrieved July 1, 2025 from https://www.ti.com/lit/an/swra553a/swra553a.pdf Application Report SWRA553A, Revision A.

[36] Stefan Uhlmann and Serkan Kiranyaz. 2013. Integrating Color Features in Polarimetric SAR Image Classification. *IEEE Transactions on Geoscience and Remote Sensing* 52, 4 (2013), 2197–2216. https://doi.org/10.1109/TGRS.2013.2258675

[37] Tristan Visentin, Wilhelm Keusgen, and Richard Weiler. 2015. Dual-polarized square-shaped offset-fed reflectarray antenna with high gain and high bandwidth in the 60 GHz domain. In *2015 9th European Conference on Antennas and Propagation (EuCAP)* (Lisbon, Portugal). IEEE, New York, NY, USA, 1–5.

[38] Timothy Woodford, Kun Qian, and Xinyu Zhang. 2024. Metasight: High-Resolution NLoS Radar with Efficient Metasurface Encoding. In *Proceedings of the 21st ACM Conference on Embedded Networked Sensor Systems* (Istanbul, Turkiye) *(SenSys '23)*. Association for Computing Machinery, New York, NY, USA, 308–321. https://doi.org/10.1145/3625687.3625803

[39] Jin Xu, Rongqiang Li, Jin Qin, Shenyun Wang, and Tiancheng Han. 2018. Ultra-broadband wide-angle linear polarization converter based on H-shaped metasurface. *Optics express* 26, 16 (2018), 20913–20919.

[40] Naoyuiki Yamada, Yuichi Tanaka, and Kunitoshi Nishikawa. 2005. Radar cross section for pedestrian in 76GHz band. In *2005 European Microwave Conference*, Vol. 2. IEEE, 4–pp.

[41] Du Yang, L-L Yang, and Lajos Hanzo. 2010. DFT-Based Beamforming Weight-Vector Codebook Design for Spatially Correlated Channels in the Unitary Precoding Aided Multiuser Downlink. In *2010 IEEE International Conference on Communications* (Cape Town, South Africa). IEEE, New York, NY, USA, 1–5. https://doi.org/10.1109/ICC.2010.5502350

[42] J Andrew Zhang, Fan Liu, Christos Masouros, Robert W Heath, Zhiyong Feng, Le Zheng, and Athina Petropulu. 2021. An overview of signal processing techniques for joint communication and radar sensing. *IEEE Journal of Selected Topics in Signal Processing* 15, 6 (2021), 1295–1315. https://doi.org/10.1109/JSTSP.2021.3113120

[43] Renjie Zhao, Timothy Woodford, Teng Wei, Kun Qian, and Xinyu Zhang. 2020. M-Cube: a millimeter-wave massive MIMO software radio. In *Proceedings of the 26th Annual International Conference on Mobile Computing and Networking* (London, United Kingdom) *(MobiCom '20)*. Association for Computing Machinery, New York, NY, USA, Article 15, 14 pages. https://doi.org/10.1145/3372224.3380892

[44] Kai Zheng, Wuqiong Zhao, Timothy Woodford, Renjie Zhao, Xinyu Zhang, and Yingbo Hua. 2024. Enhancing mmWave Radar Sensing Using a Phased-MIMO Architecture. In *Proceedings of the 22nd Annual International Conference on Mobile Systems, Applications and Services* (Minato-ku, Tokyo, Japan) *(MOBISYS '24)*. Association for Computing Machinery, New York, NY, USA, 56–69. https://doi.org/10.1145/3643832.3661865